Available online at www.sciencedirect.com
ScienceDirect
Trans. Nonferrous Met. Soc. China 34(2024) 3935−3948
Transactions of Nonferrous Metals Society of China
www.tnmsc.cn

Enhancing high-temperature oxidation resistance of nickel superalloy obtained by laser powder bed fusion via reactive electric spark treatment

S. K. MUKANOV, M. I. PETRZHIK, A. E. KUDRYASHOV, E. A. NAUMOVA, F. A. BASKOV, P. A. LOGINOV, E. A. LEVASHOV

National University of Science and Technology MISIS, Leninsky pr. 4, Moscow 119049, Russia

Received 30 August 2023; accepted 4 March 2024

Abstract: The high-temperature oxidation resistance of the nickel superalloy prepared by the laser powder bed fusion (LPBF) has been significantly increased as a result of in-situ formation of a thermal barrier layer (α-Al_2O_3 + $CaMoO_4$) during oxidative annealing of surface layers modified by electric spark treatment (EST). The reactive EST of the LPBF-built items based on nickel EP741NP alloy was carried out with low-melting Al−12%Si, Al−6%Ca−0.6%Si and Al−7%Ca−1%Mn electrodes. It was found that under EST done by Al−7%Ca−1%Mn electrode an intermetallic (β-NiAl + γ'-Ni_3Al) 15 μm-thick layer reinforced by spherical oxide (CaMe)O nanoparticles was formed. Formation of that structure increases the wear resistance of LPBF nickel superalloy by 4.5 times. Further oxidative annealing at 1000 °C leads to a formation of continuous two-layered coating with an inner layer of α-Al_2O_3 and an outer layer of $CaMoO_4$, which together act as an effective barrier preventing the diffusion of oxygen into the bulk of the superalloy.
Key words: Ni-base superalloy; laser powder bed fusion (LPBF); reactive electric spark treatment (EST); low-melting electrode; oxidation resistance; thermal barrier layer

1 Introduction

Nickel-base superalloys are widely used to manufacture critical parts of power plants operating in atmospheric air under high-temperature gas corrosion conditions, including loads [1]. Oxidation of the alloys depending on their chemical composition and microstructure starts in the temperature range of 750−800 °C, which shortens their service life and limits the scope of applications at higher temperatures [2,3]. Therefore, it is relevant to increase the operating temperatures and enhance wear resistance, which are responsible for the service life of parts made of these alloys, especially those manufactured by laser powder bed fusion (LPBF).

Most nickel-base superalloys form fast-growing oxides of nickel (NiO), chromium (CrO, CrO_2, CrO_3, and Cr_2O_3) [4] and spinels based on $NiAl_2O_4$, $NiCr_2O_4$, $(Ni,Cr)Al_2O_4$, $CoAl_2O_4$, and $NiWO_4$ [5] in air at temperatures above 750 °C. If a discontinuous surface oxide layer is formed or this layer is damaged, oxygen atoms diffuse into the bulk of the material, eventually leading to complete failure of the item. Gaseous (oxygen) corrosion is the main cause of elevated-temperature failure of structural materials. Modern understanding of the principles underlying successful protection of items against oxidation is based on ensuring conditions for the formation of thermostable phases making a dense barrier layer that prevents oxygen diffusion (i.e., on inhibiting oxide formation). The maximally efficient barrier layer is expected to consist of

Corresponding author: S. K. MUKANOV, E-mail: smukanov@misis.ru
DOI: 10.1016/S1003-6326(24)66649-5

thermally stable phases and high adhesion to the metal substrate, also contain no microcrack defects [6−8].

Ion-plasma technologies have been successfully used for depositing high-temperature barrier coatings [9,10]. However, their use is limited because of the weak adhesion of coating to the substrate. On the contrary, electrospark treatment (EST) makes it possible to form coatings with high adhesion to the substrate using electrodes made of both hard alloys [11] and low-melting eutectic-based metallic glasses [12]. So, EST is more effective for increasing the resistance of parts to wear and high-temperature oxidation.

The versatility of electric spark technologies allows one to produce composite surface layers exhibiting excellent properties. For example, in Ref. [13], vacuum electric spark and plasma arc treatment with CompoNiAl-M5-3 ($Ni_{41}Al_{41}Cr_{12}Co_6$-$Hf_{0.25}$) electrode of EP741NP alloy obtained by additive manufacturing (AM) technology were used sequentially. The double-layer coatings showed higher resistance to high-temperature oxidation in air at 1000 °C for 5 h than the substrate because of the increased Al content (up to 32 at.%) compared with that in the substrate. This can be explained by the high thermodynamic stability of aluminum oxide formed during oxidative heating [14]. As part of improving the protective coatings containing Al, modifying additives Y [4,15], Pt [16], and Cr [17] are used to accelerate the formation of stable α-Al_2O_3 oxide or improve its adhesion.

According to the Richardson–Ellingham diagram [18], calcium oxide has low Gibbs free energy like aluminum oxide does, which is indicative of its thermodynamic stability. Based on this fact, near-eutectic ternary calcium-containing electrodes Al−7%Ca−1%Mn and Al−6%Ca−0.6%Si were proposed in the earlier studies [19] for electric spark treatment of nickel alloys obtained by AM. In particular, the electrospark layer formed during EST using the Al−7%Ca−1%Mn electrode exhibited excellent oxidation resistance at 870 °C due to the formation of a dense uniform $CaAl_2O_4$ barrier layer and a high β-NiAl content. Therefore, it is especially interesting to use Ca as an alloying element to increase resistance to high-temperature oxidation at 1000 °C.

A new trend in the development of EST is elimination of surface defects typical of LPBF-built items. The high potential of using EST has been demonstrated in Refs. [19−21]. It was found that local protrusion melting takes place when using low-melting Al−Si electrodes during EST of LPBF-built items made of Ti- and Ni-based alloys and containing typical surface defects. The chemically active fluid-flow melt formed in the inter-electrode space spreads over the surface, fills the dimples, and interacts with elements from the substrate. Its solidification is accompanied by formation of intermetallic compounds, surface roughness reduction and strengthening.

This study aimed to investigate whether resistance against wear and high-temperature oxidation at 1000 °C of LPBF-built items based on nickel superalloy can be enhanced using electric spark treatment with low-melting Al−12%Si, Al−6%Ca−0.6%Si, and Al−7%Ca−1%Mn electrodes.

2 Experimental

Heat-resistant LPBF-built alloy of EP741NP grade [4] (55.38 Ni, 15.49 Co, 10.84 Al, 10.03 Cr, 2.29 Mo, 2.18 Ti, 1.75 W, 1.62 Nb, 0.19 C, 0.08 Hf, 0.08 B, 0.05 Mg, 0.017 Cr, and 0.003 Ce in at.%) was used as a substrate (cathode). Laser powder bed fusion of the EP741NP alloy was conducted on an EOS M 400 3D printer (EOS, Germany) equipped with an ytterbium-doped fiber laser. Samples were produced under an argon atmosphere with laser power of 180 W, scan speed of 800 mm/s, layer thickness of 0.04 mm, and laser spot diameter of 0.10 mm. The stripe scanning strategy without contour was applied for depositing each layer, and the scanning direction between the adjacent deposition layers was rotated by 67° [4].

Structurally homogeneous rods of 4 mm in diameter manufactured by melt quenching were used as electrodes (anode), and their compositions were as follows: Al−12%Si, Al−6%Ca−0.6%Si, and Al−7%Ca−1%Mn (mass fraction).

Electric spark treatment was carried out on an Elitron 22A automated stand in an argon atmosphere (pulse energy 1.6 mJ, pulse duration 100 μs, voltage 20 V, and pulse frequency 100 Hz). The gain in substrate mass $\Sigma\Delta K$ and electrode mass loss $\Sigma\Delta A$ were measured on a KERN 770 analytical balance (KERN, Germany).

The microstructure and composition were examined on an S−3400N scanning electron micro-

scope (Hitachi, Japan) equipped with NORAN System 7 X-ray Microanalysis (Thermo Scientific, USA) for energy dispersive spectroscopy (EDS). X-ray diffraction (XRD) phase analysis was performed using the spectra recorded on a D2 PHASER automated diffractometer (Bruker AXS, USA) using non-monochromatic Cu K_α radiation (λ=0.15418 nm). The quantitative fractions of the phases were determined using DIFFRAC. EVA (Bruker, USA) software by intelligently separating the reflexes taking into account the EDS results and then measuring their intensity.

The fine structure was studied on a JEM−2100 transmission electron microscope (TEM) (Jeol, Japan). The samples (lamellae) were cut off from the near-surface layers modified by EST using the focused ion beam technique on a Quanta 200 3D FIB instrument (FEI Company, USA). Low ionic current (10 pA) was used to reduce lamella contamination by evaporated material resulting from its condensation on metal surfaces.

High-temperature oxidation resistance tests using the sample mass gain method were carried out in a SNOL 7.2/1200 electric muffle furnace (Lithuania) at 1000 °C for 30 h in air; exposure duration was 0.25, 0.5, 0.75, 1, 2, 3, 4, and 5 h, and then every 5 h. Specific mass gain (K) was measured on an ALC-210d4 analytical balance (Acculab, USA) with an accuracy of 0.1 mg and was calculated using the following formula:

$$K=\Delta m/S_0 \quad (1)$$

where Δm is the difference between the sample mass before the test and its mass after oxidation, and S_0 is the total surface area of the sample before the test.

The oxidation rate (V) was calculated as a ratio of the specific mass gain of the sample to test duration (t):

$$V=K/t \quad (2)$$

The Gibbs free energies (ΔG) of the potential chemical reactions occurring during oxidation were calculated using the FACT software [22].

The pin-on-plate tribological reciprocating sliding tests were carried out at room temperature on a TRIBOMETER (CSM Instruments, Switzerland) in compliance with the ASTM G133-22 standard test method before and after high-temperature oxidation resistance tests. A ball with 3 mm in diameter made of 100Cr6 steel (ASTM 52100) was used as a counterbody. The test conditions were as follows: wear track length, 4 mm; applied load, 2 N; maximum speed, 5 cm/s. The wear tracks were studied using a WYKO NT1100 optical profilometer (Veeco, USA). The reduced wear (I) was calculated by normalizing the volume loss during testing (ΔV) by the mileage (N) and the applied load (P):

$$I=\frac{\Delta V}{NP} \quad (3)$$

3 Results

3.1 Characterization of substrates and electrodes

According to the XRD data (Fig. 1), the structure of the LPBF-built EP741NP sample consists of the γ-(Ni) solid solution with lattice parameter a=0.3609 nm. The near-eutectic Al−Si electrode contains two phases of (Al) solid solution and Si; Al−Ca electrodes also contain two phases of

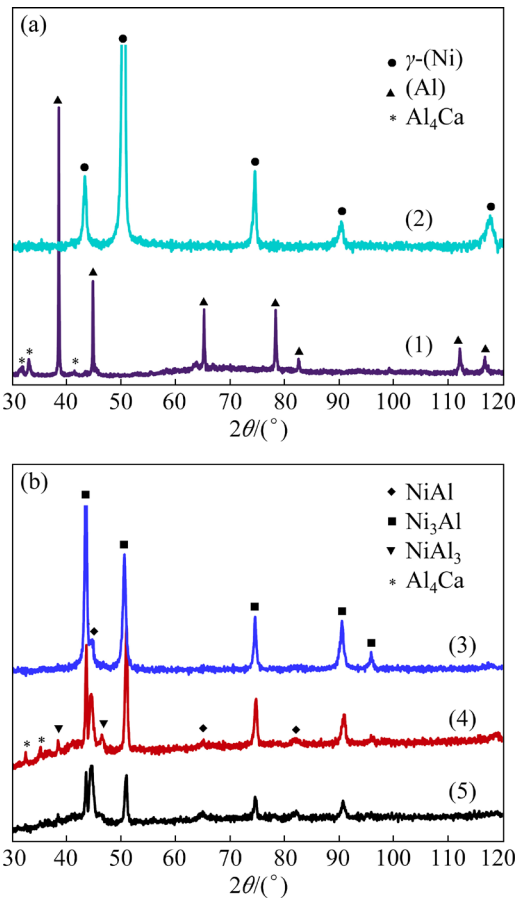

Fig. 1 XRD patterns of Al−7%Ca−1%Mn electrode (1), LPBF-built sample (2), and samples subjected to EST with Al−12%Si (3), Al−7%Ca−1%Mn (4) and Al−6%Ca−0.6%Si (5) electrodes

(Al) solid solution and Al_4Ca intermetallic phase. The portion of the Al_4Ca phase (PDF 03-065-2677) with lattice parameters a=0.4341 nm and c=1.1054 nm is 15.7 wt.%. According to the literature [23], the lattice parameter a of the Al_4Ca phase is 0.428 nm. The increase in lattice parameter a is possibly caused by substitution elements of the Al_4Ca phase by Mn in the crystal lattice.

3.2 Structure and properties of modified layers

Figure 2 demonstrates that the maximum gain in substrate mass ΔK was observed after EST with the Al−Ca−Me electrodes during 3 min. The $\sum\Delta K$ values for these electrodes were 35% higher than those recorded for treatment with the Al−Si electrode; erosion $\sum\Delta A$ of Al−Ca−Me electrodes also occurred more vigorously. Therefore, EST mode of all the samples was performed under 3 min/cm^2.

Figure 3 shows the microstructure of the modified layers and the elemental composition of structural zones after EST with low-melting Al−6%Ca−0.6%Si and Al−7%Ca−1%Mn electrodes. One can see that thickness of the layers is as high as 15 μm, and the boundary between structural components is well-discernible according to the concentration contrast and difference in the morphology.

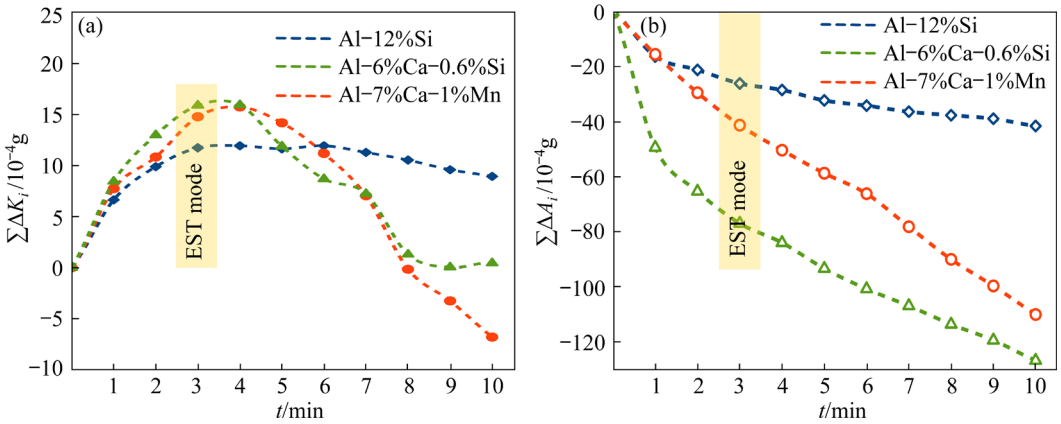

Fig. 2 Kinetic curves of mass transfer of LPBF sample with area of 1 cm^2 after EST: (a) Mass gain of substrate $\sum\Delta K$ (cathode); (b) Mass loss of electrode $\sum\Delta A$ (anode)

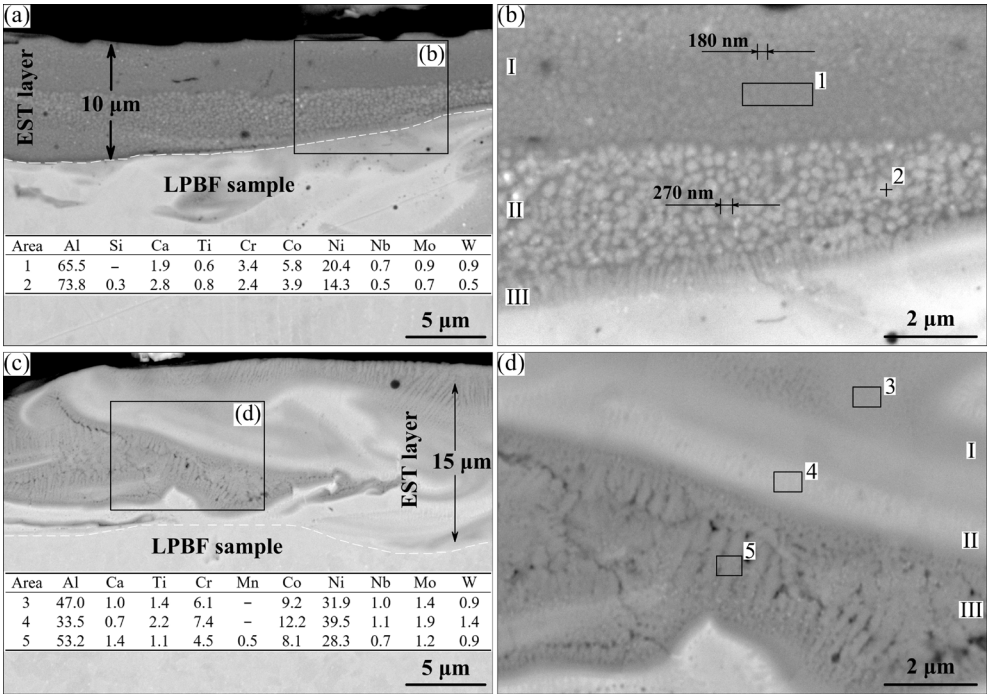

Area	Al	Si	Ca	Ti	Cr	Co	Ni	Nb	Mo	W
1	65.5	–	1.9	0.6	3.4	5.8	20.4	0.7	0.9	0.9
2	73.8	0.3	2.8	0.8	2.4	3.9	14.3	0.5	0.7	0.5

Area	Al	Ca	Ti	Cr	Mn	Co	Ni	Nb	Mo	W
3	47.0	1.0	1.4	6.1	–	9.2	31.9	1.0	1.4	0.9
4	33.5	0.7	2.2	7.4	–	12.2	39.5	1.1	1.9	1.4
5	53.2	1.4	1.1	4.5	0.5	8.1	28.3	0.7	1.2	0.9

Fig. 3 SEM images of modified layers formed after EST using Al−6%Ca−0.6%Si (a, b) and Al−7%Ca−1%Mn (c, d) electrodes and corresponding EDS data (wt.%)

The electric spark layer formed after EST with the Al−6%Ca−0.6%Si electrode (Figs. 3(a, b)) consists of two sublayers with spherical grains (I and II), as well as Zone III of columnar crystallites, with long axis oriented perpendicular to the interface with substrate. The size of spherical grains increases from 180 nm in the near-surface Zone I to 270 nm in the intermediate Zone II. Compared to Layer II, grains in Zone I contain no silicon and are depleted in aluminum and calcium, but enriched in nickel. The transversal size of crystallites in Zone III is no larger than 100 nm, while their orientation coincides with direction of heat dissipation.

As one can see in Figs. 3(c, d), EST with the Al−7%Ca−1%Mn electrode yields a lamellar structure that can be subdivided into three zones. Zones I and II consist of columnar NiAl crystallites with the transverse grain size <100 nm. A columnar structure is observed in Zone III (<1 μm in thickness). This zone was also found to have increased contents of Al (53.2 at.%), Ca (1.4 at.%) and Mn (0.5 at.%) and reduced Ni content (28.3 at.%). The $NiAl_3$ phase detected by XRD phase analysis is possibly concentrated here.

The XRD patterns (Fig. 1(b)) indicate that the modified layers consist predominantly of the intermetallic phases γ'-Ni_3Al (PDF 03-065-0430) and NiAl (PDF 01-083-3994). Furthermore, the XRD patterns shown in (4) and (5) of Fig. 1(b) (after EST with Al−Ca−Me electrodes) contained peaks belonging to $NiAl_3$, as well as weak-intensity reflections at 2θ angles of ~32°, 35° and 41° corresponding to the crystalline phase of the tetragonal system (*I*4/*mmm*), which seems to be Al_4Ca phase.

The electric spark layer formed after EST with the Al−7%Ca−1%Mn electrode was additionally analyzed by TEM. Figure 4(a) shows an image of the lamella cut off from a transverse section. One can see that equiaxed grains sized 1.0−1.5 μm reside closer to the surface, while grains located farther away from the surface have an elongated shape (up to 3.5 μm in length). Analyzing electron diffraction from the grain oriented along the [111] zone axis it was found that it has structure of β-NiAl phase (a=0.2894 nm). This finding is consistent with the XRD data. One can see from Fig. 4(b) that spherical nanoparticles, with the average size of ~20 nm, are embedded in the matrix. Dark gray "belts" in between nanoparticles have the same composition as the matrix, and their average width is <10 nm.

The phase composition of spherical nanoparticles was identified by simultaneously analyzing the EDS spectra and Fourier transforms (Fig. 5). The high calcium content in the spectra, as well as the presence of reflections from the (011) planes with interplanar distance d=0.241 nm (Fig. 5(a)) indicates that nanoparticles have a CaO-type structure. According to the EDS data (Fig. 5(b)), the nanoparticles have higher calcium and oxygen contents and lower content of the remaining elements compared to the matrix. Since spherical nanoparticles consist of 50 at.% metals (Al, Ni, Co and Cr), 30 at.% calcium and 19.4 at.% oxygen (Fig. 5(c)), it is fair to assume that they correspond to complex oxide (CaMe)O.

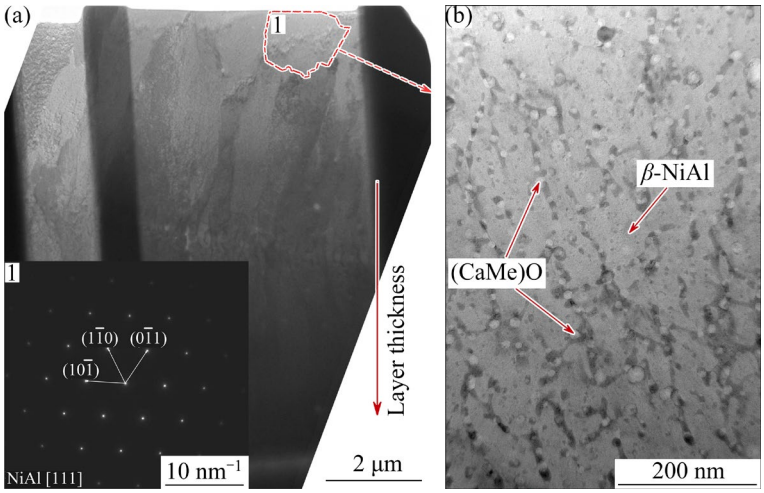

Fig. 4 TEM image of electrospark layer formed after EST with Al−7%Ca−1%Mn electrode: (a) Image of lamella and microdiffraction pattern; (b) Nanostructure of individual grain

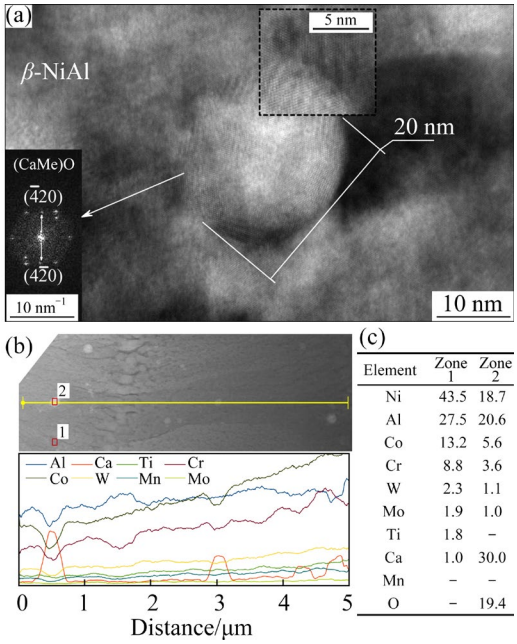

Fig. 5 (a) TEM image of spherical (CaMe)O nanoparticle in NiAl matrix formed during EST using Al−7%Ca−1%Mn electrode; (b) Element distribution over lamella thickness; (c) Corresponding EDS data (at.%)

3.3 Structure and phase transition during oxidative annealing

Figure 6(a) shows the kinetic curves of oxidation of the samples at exposure duration of 30 h. Regression analysis (Table 1) demonstrates that oxidation of the LPBF-built sample occurs via the linear law and involves two stages. During the first 4 h (the first stage) the sample mass linearly increases, and the mass gain is minimal. At the second stage, the oxidation rate increases abruptly to 3.2×10^{-4} mg/(cm^2·s), since oxygen penetration occurs, followed with formation and peeling of the oxide layer (Fig. 6(b)). In contrast, in samples subjected to EST, oxidation occurs at one stage and the formed oxide layer does not peel off (Figs. 6(c−e)).

Oxidation of the samples subjected to EST with the Al−12%Si and Al−6%Ca−0.6%Si electrodes also involves two stages. Rapid oxidation occurs initially (Table 1), further leading to oxide layer growth. The formed oxide layer acts as a barrier, i.e., it slows down the oxidation rate and the mass gain rate of the sample according to the parabolic law at exposure durations between 4 and 20 h. At exposure durations longer than 20 h, two out of three samples showed an increase in mass gain and transition to the linear oxidation law, which was caused by cracking oxide film and losing its continuity under thermal cycling conditions (Figs. 6(c, d)). The best high-temperature oxidation resistance was attained after EST with the Al−7%Ca−1%Mn electrode (Figs. 6(a, e)). Oxidation of this sample followed the parabolic law in the entire range of exposure durations.

Figure 7 and Table 2 show the phase composition of oxidized samples. Oxidation of the untreated LPBF sample gives rise to $NiMoO_4$, NiO, and $NiWO_4$ oxides. The surface layer of the sample subjected to EST using the Al−12%Si electrode

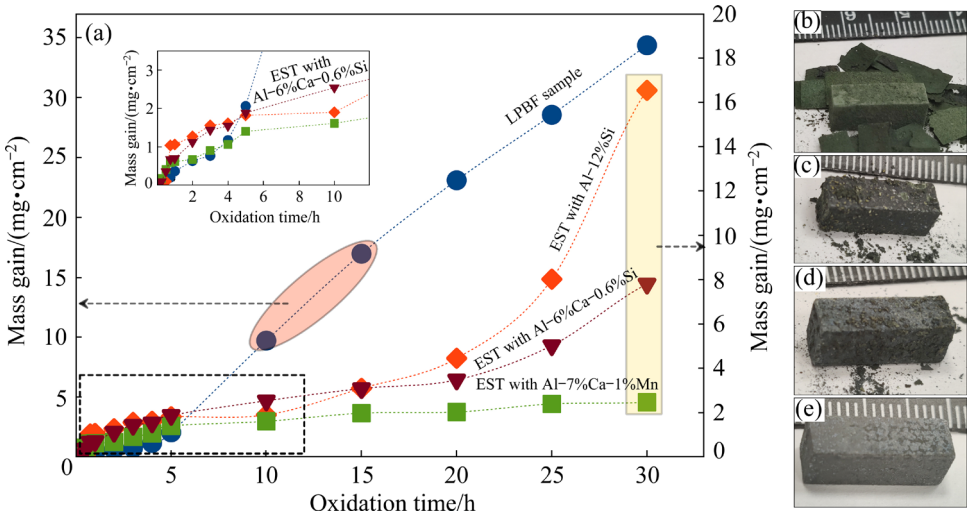

Fig. 6 Kinetic curves of sample oxidation before and after EST (a) and appearance (b−e) of samples after annealing at 1000 °C for 30 h: LPBF-built sample (b), and EST samples with Al−12%Si (c), Al−6%Ca−0.6%Si (d) and Al−7%Ca−1%Mn (e) electrodes

Table 1 Parameters of regression equation for oxidation kinetic curves at 1000 °C during 30 h

Sample	Time interval/h	Regression equation	Confidence coefficient of fitting	Oxidation rate/ (10^{-4} mg·cm^{-2}·s^{-1})
EP741NP (1)	$0 < t < 4$	$\Delta m/S=0.278t$	0.9814	0.8
	$5 \le t \le 30$	$\Delta m/S = 1.2809t$ −3.2898	0.9952	3.2 (fractured after 15 h)
(1) + EST with Al−12%Si	$0 < t <20$	$\Delta m/S= 0.9112t^{0.5}$	0.9461	1.5
	$20 \le t \le 30$	$\Delta m/S=1.2084t$ −20.539	0.9471	1.5
(1) + EST with Al−6%Ca−0.6%Si	$0 < t < 20$	$\Delta m/S=0.9385t^{0.5}$	0.9763	0.7
	$20 \le t \le 30$	$\Delta m/S=0.4321t−5.3642$	0.9737	0.7
(1) + EST with Al−7%Ca−1%Mn	$0 < t \le 30$	$\Delta m/S=0.5621t^{0.5}$	0.9805	0.2

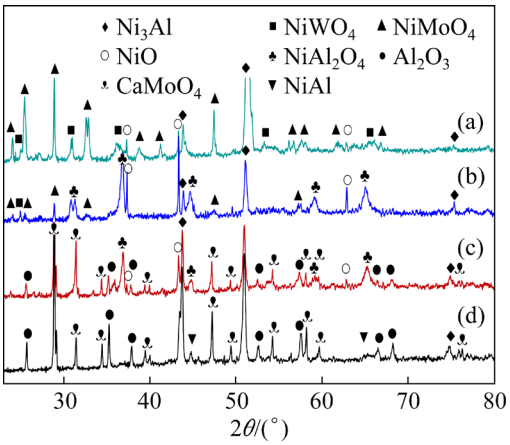

Fig. 7 XRD patterns of samples after oxidation at 1000 °C during 30 h: (a) LPBF-built sample; (b, c, d) Samples after EST with Al−12%Si, Al−6%Ca−0.6%Si, and Al−7%Ca−1%Mn, respectively

predominantly consists of $NiAl_2O_4$ phase with structure of spinel. An oxide layer consisting of α-Al_2O_3 and $CaMoO_4$ is formed during oxidative annealing of the sample subjected to EST with the Al−6%Ca−0.6%Si electrode. The XRD pattern was also found to contain low-intensity peaks corresponding to the NiO phase with the lattice parameter a=0.8353 nm. Therefore, it is fair to say that for this sample, the second stage at exposure durations of 20 h ≤ t ≤ 30 h follows the linear law (Fig. 6) and is related to oxidation of the Ni substrate. For the sample treated with the Al−7%Ca−1%Mn electrode, the content of the $CaMoO_4$ phase noticeably increases from 10.2 to 43.3 wt.% after annealing for 30 h. At this case oxidation involves a single stage and follows the parabolic law.

Figure 8 shows the morphology of the samples subjected to oxidation at 1000 °C for 30 h. Based on the analysis of both EDS and XRD (Table 2), one can suppose that the loose oxide layer with dark inclusions within the spot of the surface of sample not subject to EST consists of NiO (Fig. 8(a)). The oxidized surface of the electrospark layer with the Al−12%Si electrode mostly consists of $NiAl_2O_4$ spinel (Fig. 8(b)) as well as NiO and $NiMoO_4$ oxides, being consistent with the XRD data.

After oxidation test, the surface of the sample subjected to treatment with the Al−6%Ca−0.6%Si electrode (Fig. 8(c)) is characterized by the presence of $CaMoO_4$ grains and discontinuous Al_2O_3 layer with NiO. Contrariwise, oxidation of the sample subjected to EST with the Al−7%Ca−1%Mn electrode (Fig. 8(d)) resulted in the formation of a continuous $CaMoO_4$ layer with the scheelite-type structure, which has a fine-grained dense white- colored structure with dark inclusions of Al_2O_3. No grains of the NiO phase were detected on the surface.

Oxidative annealing on the samples subjected to EST using the Al−12%Si and Al−6%Ca−0.6%Si electrodes (Figs. 9(b, c)) was accompanied by formation of multiphase oxide layer in which light-gray areas correspond to the Mo-containing phases. Near-surface grains of NiO was detected for these samples. As it is demonstrated in the kinetic oxidation curves (Fig. 6(a)), it unfavorably affected resistance to high-temperature oxidation of the samples. Islet-like growth regions of $CaMoO_4$ grains were detected for the sample subjected to treatment with the Al−6%Ca−0.6%Si electrode.

As distance from the surface increases, the oxide layer of sample modified with the Al−7%Ca−1%Mn electrode (Figs. 9(d) and 10) consists of $CaMoO_4$ and α-Al_2O_3 grains. Next, there lies the

Table 2 Phase composition of samples subjected to oxidation at 1000 °C for 30 h

Sample	Phase	Structure type	Content/wt.%	Lattice parameter/nm		
				a	*b*	*c*
LPBF-built EP741NP (1)	$NiMoO_4$	$C2/m$	62.2	0.9566	0.8734	0.7649
	NiO	$Fm\bar{3}m$	13.4	0.8348	–	–
	$NiWO_4$	$P2/c$	12.6	0.4600	0.5660	0.4910
	Ni_3Al	$Pm\bar{3}m$	11.8	0.3569	–	–
(1) + EST with Al−12Si	$NiAl_2O_4$	$Fd\bar{3}m$	64.1	0.8106	–	–
	NiO	$Fm\bar{3}m$	17.4	0.8358	–	–
	$NiMoO_4$	$C2/m$	9.8	0.9566	0.8734	0.7649
	Ni_3Al	$Pm\bar{3}m$	8.6	0.3563	–	–
(1) + EST with Al−6Ca−0.6Si	Al_2O_3	$R\bar{3}c$	36.0	0.4759	–	1.2993
	$NiAl_2O_4$	$Fd\bar{3}m$	35.3	0.8054	–	–
	Ni_3Al	$Pm\bar{3}m$	13.1	0.3581	–	–
	$CaMoO_4$	$I4_1/a$	10.2	0.5222	–	1.1425
	NiO	$Fm\bar{3}m$	6.7	0.8353	–	–
(1) + EST with Al−7Ca−1Mn	Al_2O_3	$R\bar{3}c$	44.9	0.4752	–	1.2937
	$CaMoO_4$	$I4_1/a$	43.3	0.5203	–	1.1382
	Ni_3Al	$Pm\bar{3}m$	9.6	0.3585	–	–
	NiAl	$Pm\bar{3}m$	2.2	0.2860	–	–

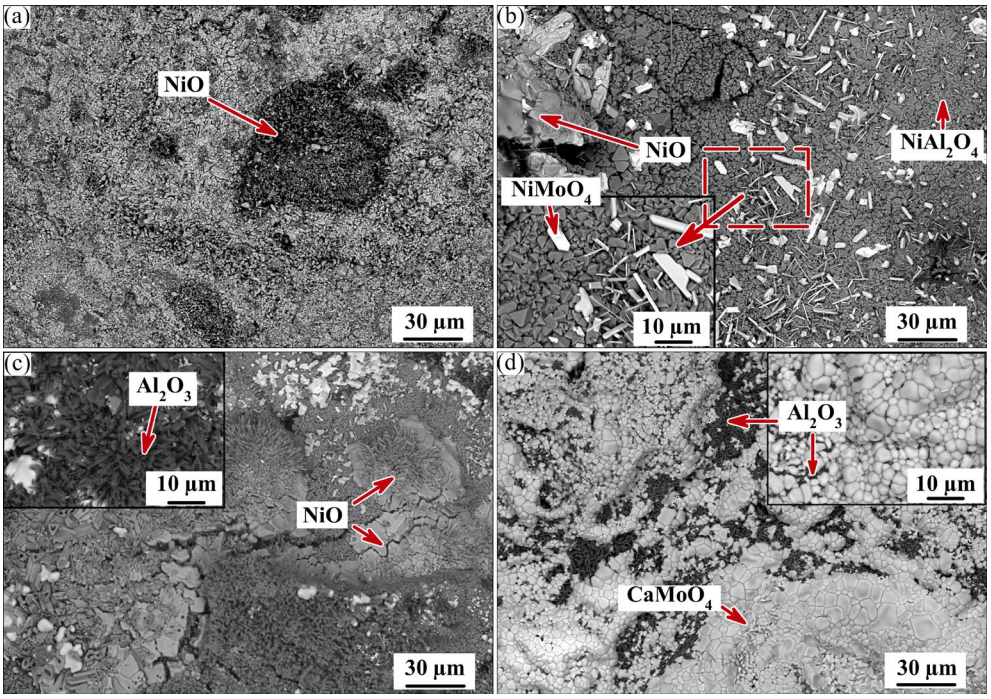

Fig. 8 SEM images of surface of samples oxidized at 1000 °C during 30 h: as-built LPBF sample (a), and samples subjected to EST using Al−12%Si (b), Al−6%Ca−0.6%Si (c) and Al−7%Ca−1%Mn (d) electrodes

oxygen-free zone rich in Ni and depleted in Al (γ'-Ni_3Al) under the oxide layer. Under it, there is a dense β-NiAl-containing layer.

In order to understand the mechanism of single-stage oxidation (according to the parabolic law) of the sample with a coating deposited using

the Al−7%Ca−1%Mn electrode, we studied the phase composition and surface morphology depending on duration (4, 10 and 30 h) of isothermal exposure at 1000 °C. At the initial oxidation stage (t=0−4 h) when continuous oxide layers were formed (1.068 mg/cm^2), the mass gain sample was minimal. After annealing for 30 h, the mass gain was 2.474 mg/cm^2, being noticeably lower than that for other samples.

Figure 11 shows that intensity of XRD peaks corresponding to β-NiAl decreases with increasing oxidation duration, while the intensity of α-Al_2O_3 and $CaMoO_4$ peaks increases in a regular manner. Hence, β-NiAl accumulates Al, and the α-Al_2O_3 layer is formed on the surface after the β-NiAl → γ'-Ni_3Al phase transition. The surface morphology of the samples (Fig. 11(b)) demonstrated that grains of $CaMoO_4$ were formed as early as after isothermal exposure for 4 h. Continuity of the layer increased with oxidation duration.

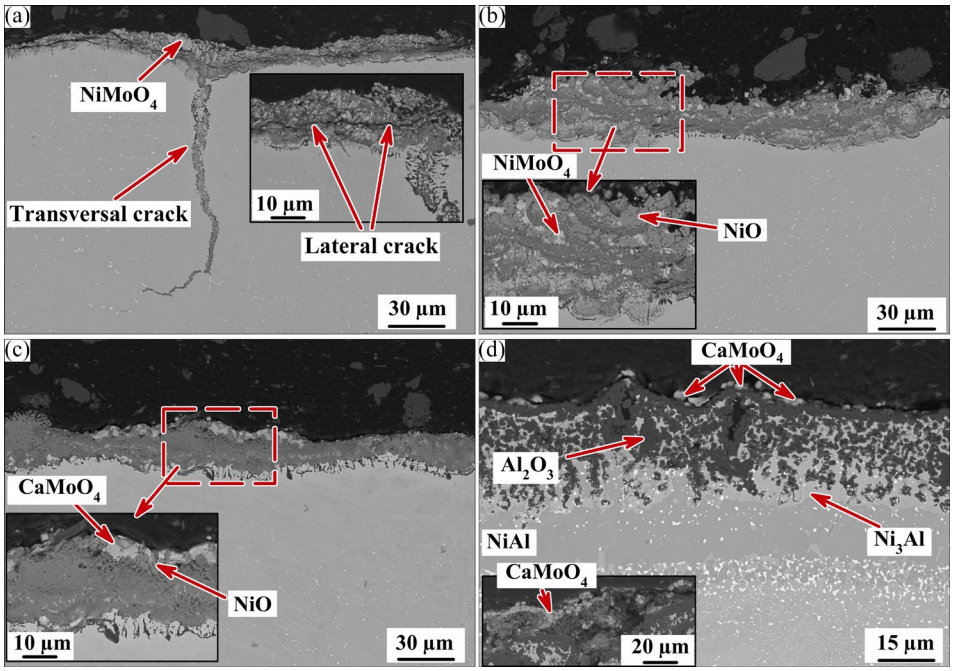

Fig. 9 SEM images of transverse sections of samples after high-temperature oxidation resistance tests at 1000 °C for 30 h in air: as-built LPBF sample (a), and samples subjected to EST using Al−12%Si (b), Al−6%Ca−0.6%Si (c) and Al−7%Ca−1%Mn (d) electrodes

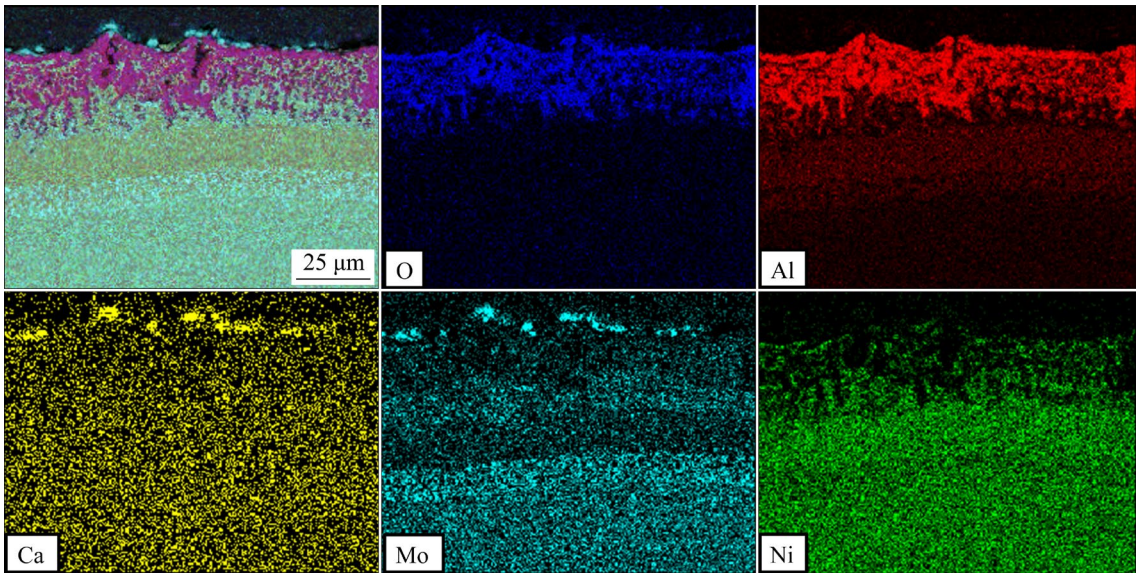

Fig. 10 Element distribution map for transverse section of oxidized sample subjected to EST using Al−7%Ca−1%Mn electrode

3.4 Tribological behavior after oxidative annealing

Figure 12 shows the effect of oxidative annealing on wear resistance of the EP741NP alloy subjected to EST. As temperature and duration of oxidative annealing rose, wear resistance of the EP741NP alloy and modified layers formed using the Al−12%Si and Al−6%Ca−0.6%Si electrodes increased noticeably due to the formation of hard oxide layers. Reduced wear of oxidized coatings was 7.72×10^{-5} and 9.21×10^{-5} mm^3/(N·m) for the Al−12%Si and Al−6%Ca−0.6%Si electrodes, respectively, being lower than that for the unprotected EP741NP (11.8×10^{-5} mm^3/(N·m)). It can be related to spalling of loose nickel oxide layers during tribological tests and their grinding in the wear area. As one can see from Fig. 12 for all

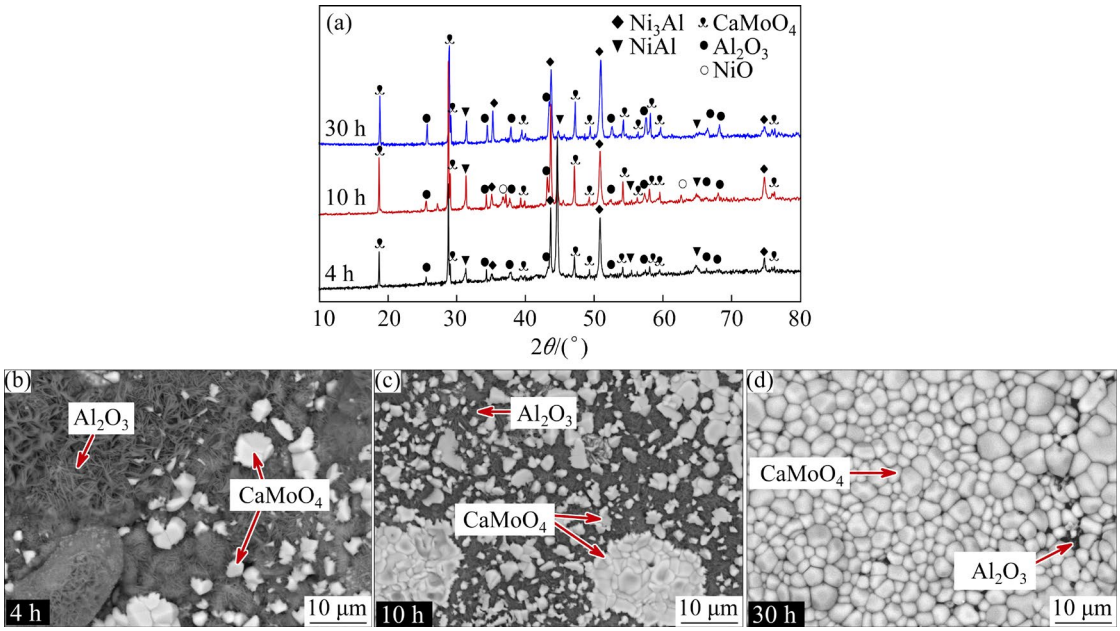

Fig. 11 XRD patterns (a) and morphologies (b−d) of electrospark layer formed by EST with Al−7%Ca−1%Mn electrode after oxidation at 1000 °C for 4, 10 and 30 h, respectively

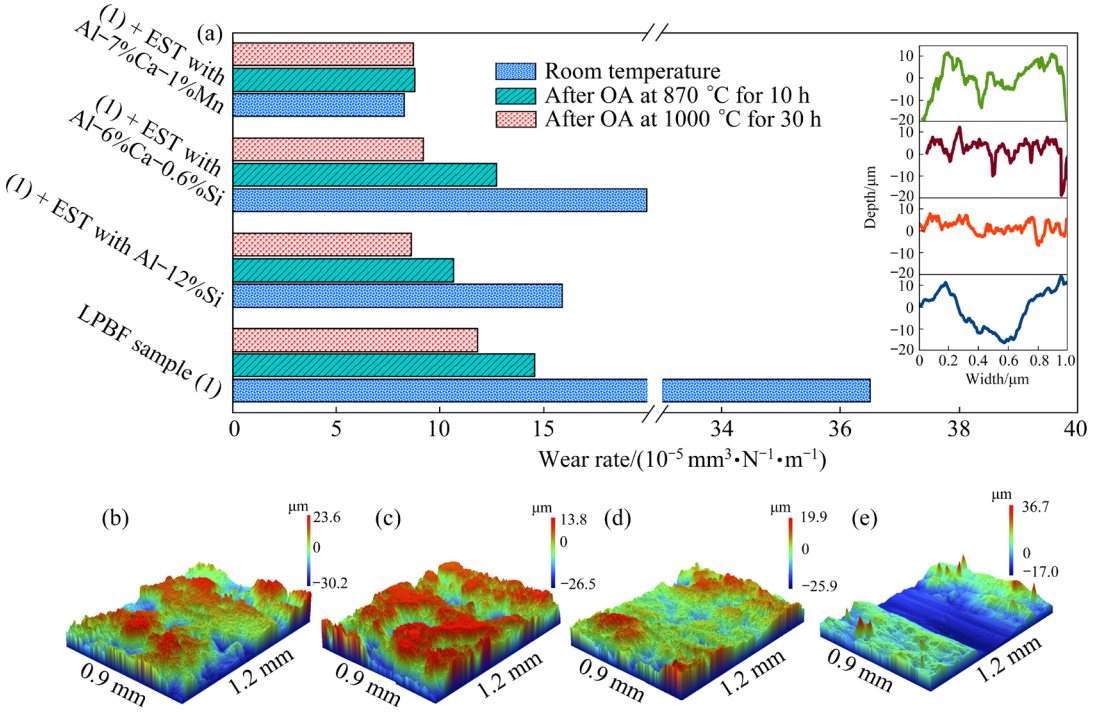

Fig. 12 Reduced wear of samples subjected to EST before and after oxidation annealing (OA) at 870 and 1000 °C (in inset there are profiles of wear tracks of samples after OA at 1000 °C) (a); 3D images of wear tracks: (1) + EST with Al−7%Ca−1%Mn (b), (1) + EST with Al−6%Ca−0.6%Si (c), (1) + EST with Al−12%Si (d), and LPBF sample (e)

the samples subjected to EST the values of reduced wear after oxidative annealing at 1000 °C virtually coincide. However, a formation of $CaMoO_4$ and Al_2O_3 at the surface layer modified with Al−7%Ca−1%Mn electrode was found after 30 h exposure. It was accompanied by slight increase of reduced wear from 8.29×10^{-5} to 8.71×10^{-5} $mm^3/(N\cdot m)$.

4 Discussion

The experimental findings reported in Section 3.2 prove that EST of LPBF-built Ni-based sample using low-melting Al−Si and Al−Ca−Me electrodes altered the phase composition of the surface layers due to reactive phase formation. Mixing of elements at conditions of the local melting and high cooling rates [12] during EST of the γ-Ni alloy contributed to formation of the matrix consisting of intermetallic β-NiAl and γ'-Ni_3Al phases strengthened by spherical nanoparticles of (MeCa)O-type complex oxide. Since EST took place in the flow of protective argon gas and oxygen content in the particle was ~20%, it is fair to assume that calcium had reduced metal oxides (e.g., via reaction MeO+Ca = CaO+Me). Spherical shape of particles and their incoherence with the matrix indicate that CaO particles were formed either in the gas flow or in the melted drop. These particles seem to be stronger than the β-NiAl intermetallic phase (the matrix), since they retain their shape after melt solidification, thus strengthening the modified layer. As it has been found in Section 3.2, the "belts" connecting the nanoparticles are <10 nm wide, which do not differ from the matrix in their elemental composition, and possibly are the shear bands.

According to the XRD data, EST was accompanied by enrichment in aluminum of the surface of the Ni alloy. It promoted the formation of $NiAl_3$. LI et al [24] revealed similar behavior when treated TiAl alloy with an Al electrode. However, in our study, formation of $NiAl_3$ was observed only under EST using the Al−Ca−Me electrodes. This can be attributed to the presence of Al_4Ca intermetallic phase in the eutectic system [23], which undergoes peritectic melting at a relatively low temperature of 700 °C, thus increasing erosion compared with the case of the Al−Si electrode (Fig. 2).

The $NiAl_3$ phase in the modified layer is a source of aluminum that is required for the protective α-Al_2O_3 diffusion layer to be formed during oxidative annealing. With allowance for the experimental data, the oxidation mechanism of nickel alloy treated with the Al−7%Ca−1%Mn electrode during isothermal exposure to 1000 °C in air during 30 h is schematically shown in Fig. 13.

Selective oxidation of aluminum [25] takes place during the initial stage of isothermal exposure (t = 0−4 h), giving rise to α-Al_2O_3 via Reactions (4) and (5) [22]. This process is accompanied by a high oxidation rate, and then it begins to slow down as a continuous barrier layer impeding oxygen diffusion into the modified layer is formed.

$$NiAl_3(s)+1.5O_2(g)\rightarrow Al_2O_3(s)+NiAl(s),\quad \Delta G=-1253.5\ kJ/mol \tag{4}$$

$$3NiAl(s)+1.5O_2(g)\rightarrow Al_2O_3(s)+Ni_3Al(s),\quad \Delta G=-1098.1\ kJ/mol \tag{5}$$

$$Mo(s)+1.5O_2(g)\rightarrow MoO_3(g),\quad \Delta G=-439.3\ kJ/mol \tag{6}$$

$$MoO_3(g)+CaO(s)\rightarrow CaMoO_4(s),\quad \Delta G=-163.0\ kJ/mol \tag{7}$$

$$NiO(s)+Al_2O_3(s)\rightarrow NiAl_2O_4(s),\quad \Delta G=-25.1\ kJ/mol \tag{8}$$

As shown in Fig. 6, the Al_2O_3 layer (Al−12%Si and Al−6%Ca−0.6%Si samples) starts fracturing after isothermal exposure at t=20 h, which is accompanied by formation of a microgradient structure with precipitated $NiAl_2O_4$, NiO, and $NiMoO_4$ spinels (Fig. 9). The absence of the aluminum oxide phase on the surface of the modified layer formed using the Al−12%Si electrode can be attributed to complete dissolution in $NiAl_2O_4$ spinel as a result of interaction between aluminum oxide and nickel via chemical Reaction (8) [26].

It is fair to assume that formation of a continuous barrier consisting of $CaMoO_4$ grains tightly adjacent to each other on top of Al_2O_3 is the reason for retaining the surface layer integrity during annealing of the electrospark layer formed with the Al−7%Ca−1%Mn electrode. According to the XRD data, calcium molybdate ($CaMoO_4$) has a tetragonal scheelite-type structure having space group $I4_1/a$. This structure is characterized by high packing density in the crystal lattice, which prevents oxygen diffusion.

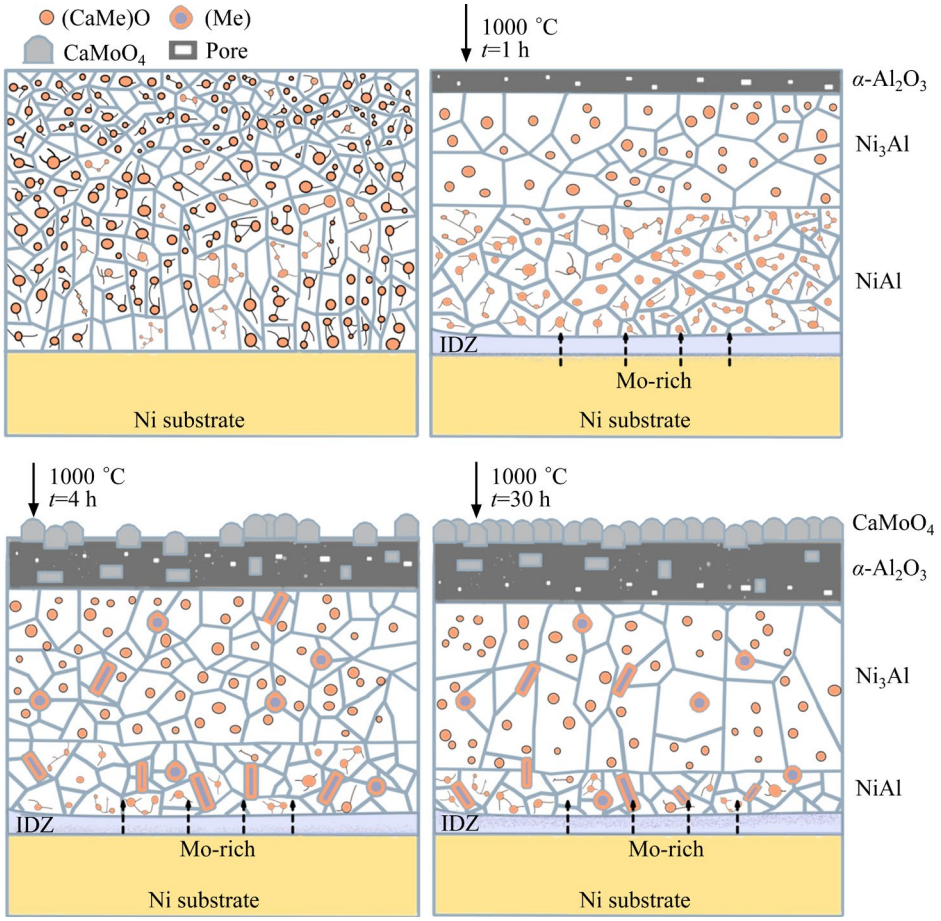

Fig. 13 Scheme of oxidation of nickel alloy with modified layer formed during EST using Al−7%Ca−1%Mn electrode

According to structural studies (Figs. 9(d) and 10), during annealing molybdenum resides along the boundary between the electrospark layer and the substrate (the interdiffusion zone, IDZ). As reported in Refs. [27−29], refractory elements (such as Mo, W and Ta) reduce high-temperature oxidation resistance of the alloys because of their diffusion to the surface layers [30]. Oxides of refractory elements (MoO_3, WoO_3 and Ta_2O_5) are usually sublimated at temperatures above 800 °C, which disrupts the oxide layer integrity. In this case, however, calcium oxide presenting in the modified layer (Figs. 4 and 5) interacts with MoO_3 to form a continuous thermally stable $CaMoO_4$ barrier layer on top of Al_2O_3 via Eqs. (4)−(7). This oxide layer increases high-temperature oxidation resistance (at 1000 °C) of nickel superalloy grown by laser powder bed fusion.

5 Conclusions

(1) Modified near-surface layers with a thickness of about 15 μm containing intermetallics were formed during reactive electric spark treatment of the LPBF EP741NP nickel alloy using low-melting electrodes (Al−12%Si, Al−6%Ca−0.6%Si and Al−7%Ca−1%Mn).

(2) The most interesting result of the EST is the formation of an intermetallic (β-NiAl + γ'-Ni_3Al) layer reinforced with spherical nanoparticles of oxide (CaMe)O in a result of the electric spark interaction of a nickel substrate and an Al−7%Ca−1%Mn electrode.

(3) The formation of nanostructured modified layer increases the wear resistance of the EP741NP alloy by 4.5 times.

(4) At further annealing during 30 h at 1000 °C in air the modified layer demonstrates the lowest oxidation rate of 0.2×10^{-4} mg/(cm^2·s) obeying the parabolic law, which is 16-fold lower than that for the unprotected EP741NP LPBF substrate (3.2×10^{-4} mg/(cm^2·s) obeying the linear law.

(5) The reason for this unusual oxidative resistance is the in-situ formation of a double barrier layer (the inner layer of α-Al_2O_3 and the outer layer of $CaMoO_4$), which prevents oxygen

penetration into LPBF EP741NP.

CRediT authorship contribution statement

S. K. MUKANOV: Investigation, Writing − Review and editing, Writing − Original draft preparation, Visualization; **M. I. PETRZHIK:** Conceptualization, Investigation, Writing − Review and editing; **A. E. KUDRYASHOV:** Investigation, Methodology, Formal analysis; **E. A. NAUMOVA:** Investigation, Formal analysis; **F. A. BASKOV:** Methodology, Resources; **P. A. LOGINOV:** Methodology, Validation, Investigation; **E. A. LEVASHOV:** Conceptualization, Funding acquisition, Writing − Review and editing, Supervision.

Declaration of competing interest

The authors declare that they have no known competing financial interests or personal relationships that could have appeared to influence the work reported in this paper.

Acknowledgments

This work was supported by the Ministry of Science and Higher Education of the Russian Federation under State Research Assignment (No. 0718-2020-0034), and Development Program of MISIS (No. K7-2023-009) within the Framework Strategic Academic Leadership Program "Priority-2030".

References

[1] HOSSEINI E, POPOVICH V A. A review of mechanical properties of additively manufactured Inconel 718 [J]. Additive Manufacturing, 2019, 30: 100877. doi.org/10.1016/j.addma.2019.100877.

[2] BOLELLI G, VORKÖTTER C, LUSVARGHI L, MORELLI S, TESTA V, VAßEN R. Performance of wear resistant MCrAlY coatings with oxide dispersion strengthening [J]. Wear, 2020, 444/445: 203116. doi.org/10.1016/j.wear.2019.203116.

[3] SUN B, ZHANG T B, SHI J Q, WANG B, ZHANG X H. Microstructural evolution during exposure in air and oxidation behavior of a nickel-based superalloy [J]. Vacuum, 2021, 183: 109801. doi.org/10.1016/j.vacuum.2020.109801.

[4] BASKOV F A, SENTYURINA Z A, KAPLANSKII Y Y, LOGACHEV I A, SEMERICH A S, LEVASHOV E A. The influence of post heat treatments on the evolution of microstructure and mechanical properties of EP741NP nickel alloy produced by laser powder bed fusion [J]. Materials Science and Engineering A, 2021, 817: 141340. doi.org/10.1016/j.msea.2021.141340.

[5] LIU C T, MA J, SUN X F. Oxidation behavior of a single-crystal Ni-base superalloy between 900 and 1000 °C in air [J]. Journal of Alloys and Compounds, 2010, 491: 522−526. doi.org/10.1016/j.jallcom.2009.10.261.

[6] WU Y, NARITA T. Oxidation behavior of the single crystal Ni-based superalloy at 900 °C in air and water vapor [J]. Surface and Coatings Technology, 2007, 202: 140−145. doi.org/10.1016/j.surfcoat.2007.05.018.

[7] GLEESON B M. Thermodynamics and theory of external and internal oxidation of alloys [M]//Shreir's Corrosion. Amsterdam: Elsevier, 2010: 180−194. doi.org/10.1016/B978-044452787-5.00012-3.

[8] XIE Yu-jiang, WANG De, WANG Ming-sheng, YE Wei. Evaluation of three kinds of MCrAlY coatings produced by electrospark deposition [J]. Transactions of Nonferrous Metals Society of China, 2016, 26: 1647−1654. doi.org/10.1016/S1003-6326(16)64274-7.

[9] GLÓRIA R F, CHAIA N, CRUZ A W, ALCKMIN L B, NUNES C A, RODRIGUES G. Aluminide coating on Mar-M246 nickel superalloy by halide activated pack cementation (HAPC) [J]. Surface and Coatings Technology, 2021, 411: 126999. doi.org/10.1016/j.surfcoat.2021.126999.

[10] BRANDL W, TOMA D, GRABKE H J. The characteristics of alumina scales formed on HVOF-sprayed MCrAlY coatings [J]. Surface and Coatings Technology, 1998, 108/109: 10−15. doi.org/10.1016/S0257-8972(98)00613-6.

[11] ZAMULAEVA E I, LEVASHOV E A, KUDRYASHOV A E, VAKAEV P V, PETRZHIK M I. Electrospark coatings deposited onto an Armco iron substrate with nano- and microstructured WC−Co electrodes. Deposition process, structure, and properties [J]. Surface and Coatings Technology, 2008, 202: 3715−3722. doi.org/10.1016/j.surfcoat.2008.01.008.

[12] PETRZHIK M, MOLOKANOV V, LEVASHOV E. On conditions of bulk and surface glass formation of metallic alloys [J]. Journal of Alloys and Compounds, 2017, 707: 68−72. doi.org/10.1016/j.jallcom.2016.12.293.

[13] SHEVEYKO A N, KUPTSOV K A, KIRYUKHANTSEV-KORNEEV P V, KAPLANSKY Y Y, OREKHOV A S, LEVASHOV E A. Protective coatings for LPBF Ni-based superalloys using a combination of electrospark deposition and pulsed arc evaporation methods [J]. Applied Surface Science, 2022, 581: 152357. doi.org/10.1016/j.apsusc.2021.152357.

[14] LONG H, MAO S, LIU Y, ZHANG Z, HAN X. Microstructural and compositional design of Ni-based single crystalline superalloys—A review [J]. Journal of Alloys and Compounds, 2018, 743: 203−220. doi.org/10.1016/j.jallcom.2018.01.224.

[15] GUO H B, GONG S K, KHOR K A, XU H B. Effect of thermal exposure on the microstructure and properties of EB-PVD gradient thermal barrier coatings [J]. Surface and Coatings Technology, 2003, 168: 23−29. doi.org/10.1016/S0257-8972(02)00925-8.

[16] SHIRVANI K, FIROUZI S, RASHIDGHAMAT A. Microstructures and cyclic oxidation behaviour of Pt-free and low-Pt NiAl coatings on the Ni-base superalloy Rene-80 [J]. Corrosion Science, 2012, 55: 378−384. doi.org/10.1016/j.corsci.2011.10.037.

[17] KITAOKA S, KUROYAMA T, MATSUMOTO M, KITAZAWA R, KAGAWA Y. Control of polymorphism in Al_2O_3 scale formed by oxidation of alumina-forming alloys [J]. Corrosion Science, 2010, 52: 429−434. doi.org/10.1016/j.corsci.2009.09.031.

[18] ARROYO-DE DOMPABLO M E, PONROUCH A, JOHANSSON P, PALACÍN M R. Achievements, challenges, and prospects of calcium batteries [J]. Chemical Reviews, 2020, 120: 6331−6357. doi.org/10.1021/acs.chemrev.9b00339.

[19] MUKANOV S K, BASKOV F A, PETRZHIK M I, LEVASHOV E A. Electro-spark treatment with low-melting Al−Si and Al−Ca electrodes in order to improve wear and oxidation resistance of EP741NP alloy prepared by selective laser melting [J]. Metallurgist, 2022, 66: 317−326. doi.org/10.1007/s11015-022-01331-0.

[20] ENRIQUE P D, MARZBANRAD E, MAHMOODKHANI Y, JIAO Z, TOYSERKANI E, ZHOU N Y. Surface modification of binder-jet additive manufactured Inconel 625 via electrospark deposition [J]. Surface and Coatings Technology, 2019, 362: 141−149. doi.org/10.1016/j.surfcoat.2019.01.108.

[21] MUKANOV S K, KUDRYASHOV A E, PETRZHIK M I. Surface modification of titanium VT6 alloy obtained by additive technologies using reactive electrospark treatment [J]. Inorganic Materials: Applied Research, 2022, 13: 732−739. doi.org/10.1134/S2075113322030261.

[22] BALE C W, BÉLISLE E, CHARTRAND P, DECTEROV S A, ERIKSSON G, GHERIBI A E, HACK K, JUNG I H, KANG Y B, MELANÇON J, PELTON A D, PETERSEN S, ROBELIN C, SANGSTER J, SPENCER P, VAN ENDE M A. Reprint of: FactSage thermochemical software and databases [J]. Calphad, 2016, 55: 1−19. doi.org/10.1016/j.calphad.2016.07.004.

[23] NAUMOVA E, DOROSHENKO V, BARYKIN M, SVIRIDOVA T, LYASNIKOVA A, SHURKIN P. Hypereutectic Al−Ca−Mn−(Ni) alloys as natural eutectic composites [J]. Metals, 2021, 11: 890. doi.org/10.3390/met11060890.

[24] LI Z W, GAO W, YOSHIHARA M, HE Y D. Improving oxidation resistance of Ti_3Al and TiAl intermetallic compounds with electro-spark deposit coatings [J]. Materials Science and Engineering A, 2003, 347: 243−252. doi.org/10.1016/S0921- 5093(02)00595-6.

[25] GRABKE H J. Oxidation of NiAl and FeAl [J]. Intermetallics, 1999, 7: 1153−1158. doi.org/10.1016/S0966-9795(99)00037-0.

[26] PENG J, FANG X F, QU Z, WANG J J. Isothermal oxidation behavior of NiAl and NiAl−(Cr,Mo) eutectic alloys [J]. Corrosion Science, 2019, 151: 27−34. doi.org/10.1016/j.corsci.2019.02.011.

[27] ZHOU B Y, HE J, LIU L, WANG S X, SUN J Y, WEI L L, GUO H B. The interaction between Dy, Pt and Mo during the short-time oxidation of (γ' + β) two-phase NiAl coating on single crystal superalloy with high Mo content [J]. Surface and Coatings Technology, 2022, 430: 127999.doi.org/10.1016/ j.surfcoat.2021.127999.

[28] WANG J L, CHEN M H, YANG L L, SUN W Y, ZHU S L, WANG F H. Nanocrystalline coatings on superalloys against high temperature oxidation: A review [J]. Corrosion Communications, 2021, 1: 58−69. doi.org/10.1016/j.corcom.2021.06.003.

[29] WANG C J, CHEN S M. Microstructure and cyclic oxidation behavior of hot dip aluminized coating on Ni-base superalloy Inconel 718 [J]. Surface and Coatings Technology, 2006, 201: 3862−3866. doi.org/10.1016/j. surfcoat.2006.07.242.

[30] ZHANG P M, LI X H, MOVERARE J, PENG R L. The iron effect on oxidation and interdiffusion behaviour in MCrAlX coated Ni-base superalloys 718 [J]. Materials & Design, 2019, 166: 107599. doi.org/10.1016/j.matdes.2019.107599.

反应电火花提高激光粉末床熔融镍基高温合金的高温抗氧化性

S. K. MUKANOV, M. I. PETRZHIK, A. E. KUDRYASHOV,
E. A. NAUMOVA, F. A. BASKOV, P. A. LOGINOV, E. A. LEVASHOV

National University of Science and Technology MISIS, Leninsky pr. 4, Moscow 119049, Russia

摘　要：采用电火花处理(EST)对激光粉末床熔融(LPBF)制备的镍基高温合金表面进行改性，由于在氧化退火过程中合金的表面原位形成了热障层(α-Al_2O_3+$CaMoO_4$)，从而显著提高了其高温抗氧化性能。使用低熔点的 Al−12%Si、Al−6%Ca−0.6%Si 和 Al−7%Ca−1%Mn 电极材料，对基于 EP741NP 镍基合金的 LPBF 样品进行 EST 处理。结果发现，当采用 Al−7%Ca−1%Mn 电极进行 EST 处理时，形成了厚约 15 μm 的球形氧化物(CaMe)O 纳米颗粒增强金属间化合物(β-NiAl+γ'-Ni_3Al)层。该结构的形成使 LPBF 镍基高温合金的耐磨性提高了 4.5 倍。进一步在 1000 ℃下进行氧化退火，合金表面形成了连续的双层涂层，其内层为 α-Al_2O_3，外层为 $CaMoO_4$。这两层共同作用，可有效阻止氧气向合金体内扩散。

关键词：Ni 基高温合金；激光粉末床熔融(LPBF)；反应电火花处理(EST)；低熔点电极；抗氧化性能；热障涂层

(Edited by Xiang-qun LI)